

Article

High-Rate Layered Cathode of Lithium-Ion Batteries through Regulating Three-Dimensional Agglomerated Structure

Jun-Ping Hu ¹, Hang Sheng ¹, Qi Deng ¹, Qiang Ma ¹, Jun Liu ¹, Xiong-Wei Wu ^{1,*}, Jun-Jie Liu ^{1,2,*} and Yu-Ping Wu ^{2,*} 

¹ School of Chemistry and Materials Science, Hunan Agricultural University, Changsha 410128, China; hjp864569039@163.com (J.-P.H.); hangsheng@iccas.ac.cn (H.S.); dengqibq@163.com (Q.D.); maqiangkq@outlook.com (Q.M.); liujunhnydx@163.com (J.L.)

² School of Energy Science and Engineering, Nanjing Tech University, Nanjing 211816, China

* Correspondence: wxw@hunau.edu.cn (X.-W.W.); 18390915816@163.com (J.-J.L.); wuyyp@njtech.edu.cn (Y.-P.W.)

Received: 17 January 2020; Accepted: 28 March 2020; Published: 1 April 2020



Abstract: $\text{LiNi}_x\text{Co}_y\text{Mn}_z\text{O}_2$ (LNCM)-layered materials are considered the most promising cathode for high-energy lithium ion batteries, but suffer from poor rate capability and short lifecycle. In addition, the $\text{LiNi}_{1/3}\text{Co}_{1/3}\text{Mn}_{1/3}\text{O}_2$ (NCM 111) is considered one of the most widely used LNCM cathodes because of its high energy density and good safety. Herein, a kind of NCM 111 with semi-closed structure was designed by controlling the amount of urea, which possesses high rate capability and long lifespan, exhibiting $140.9 \text{ mAh}\cdot\text{g}^{-1}$ at $0.85 \text{ A}\cdot\text{g}^{-1}$ and $114.3 \text{ mAh}\cdot\text{g}^{-1}$ at $1.70 \text{ A}\cdot\text{g}^{-1}$, respectively. The semi-closed structure is conducive to the infiltration of electrolytes and fast lithium ion-transfer inside the electrode material, thus improving the rate performance of the battery. Our work may provide an effective strategy for designing layered-cathode materials with high rate capability.

Keywords: agglomerated structure; high-rate; layered cathode; lithium-ion batteries

1. Introduction

Driven by the demands of increasing power density, achieving long cycle life and guaranteed safety for the next-generation lithium-ion battery in practical application, extensive research has been focus on the high performance cathodes materials [1–5]. Since the layered $\text{LiNi}_x\text{Co}_y\text{Mn}_z\text{O}_2$ ($x + y + z = 1$, LNCM) cathodes materials was put forward by J.R. Dahn, it was regarded as the most promising cathode because of the large theoretical capacity of $273 \text{ mAh}\cdot\text{g}^{-1}$ to $285 \text{ mAh}\cdot\text{g}^{-1}$, the high-voltage platform of 3.6 V and a considerable compacted density with greater than 2.6 g cm^{-3} [6–9]. And the Li-ion battery can be served as a power source for vehicle application or energy storage, which will improve the environment and accelerate development of the new energy resources [10].

Therefore, the LNCM has achieved much attention for further improving electrochemical performance [11–13]. Its intrinsic thermodynamic property can be controlled by adjusting transition metal element ratio that the nickel, manganese and cobalt ion (Ni^{2+} , Ni^{3+} , Mn^{4+} , Co^{3+}) are both occupied on the transition metal sites [14–16]. As found in previous research, the manganese element can enhance thermo-safety but has no electrochemical activity; the cobalt element can stabilize the layered structure and the nickel element mainly contributes to the specific capacity [17–19]. In order to obtain higher energy density, LNCMs with high nickel content, such as NCM 523, NCM 622, NCM 811, were studied [20–22]. Nevertheless, the increase of nickel content may sacrifice the structural stability, cycle and safety performance of LNCM. For example, $\text{LiNi}_{0.8}\text{Co}_{0.1}\text{Mn}_{0.1}\text{O}_2$ (NCM 811) cathode has a high nickel content, which can obtain a practical discharge capacity of $200 \text{ mAh}\cdot\text{g}^{-1}$. But the

unstable structure and strong side reactions with electrolyte easily results in a poor cycle performance and a hidden danger for NCM 811 [15,23]. As manganese is much cheaper than cobalt, the Li-rich manganese-based cathode materials of $x\text{Li}_2\text{MnO}_3 \cdot (1-x)\text{LiMO}_2$ with high energy density were proposed. However, it is still limited by a high-voltage platform for activation in first charging process, voltage fade and irreversible oxygen release [19,24]. Thus, it is necessary to develop LNCM which possesses a suitable element ratio to deliver excellent performances including safety, cycle-life, energy density in lithium ion batteries.

For now, $\text{LiNi}_{1/3}\text{Co}_{1/3}\text{Mn}_{1/3}\text{O}_2$ (NCM 111) possesses a high energy density, a good safety performance and a long cycle life, which is served as one of the most widely used cathode materials in electric vehicles and hybrid electric vehicles now. However, the performance of NCM 111 still can be improved to meet the demand of high power-density and rate capability for power battery through regulating its structure and morphology. And the research of zero-dimensional hollow microspheres, one-dimensional nanofibers, two-dimensional nanosheets and so on, is flourishing in recent years [25]. For example, Peng et al. synthesized three types of self-assembled NCM 111 nanosheet cathodes with different surface structures and packing degrees via hydrothermal reaction followed by a stepwise calcination process. Zheng et al. reported self-assembled NCM 111 nanosheets by a combined co-precipitation with hydrothermal method, which exhibited a discharge capacity of $155 \text{ mAh}\cdot\text{g}^{-1}$ after 1000 cycles at $0.17 \text{ A}\cdot\text{g}^{-1}$ [26–29]. In general, shortening the diffusion path of Li^+ through controlling the morphology of materials is an effective way to improve electrochemical performance for layered NCM cathodes [30].

It has been previously reported that urea can be used as a precipitator in hydrothermal treatment to construct samples of different morphologies [31–34]. In this work, three-dimensional agglomerated structures from unclosed to blocking sphere-shaped microstructure for NCM 111 were designed by controlling the contents of urea to get excellent electrochemical performance.

2. Experimental

2.1. Synthesis of $\text{LiNi}_{1/3}\text{Co}_{1/3}\text{Mn}_{1/3}\text{O}_2$

$\text{LiNi}_{1/3}\text{Co}_{1/3}\text{Mn}_{1/3}\text{O}_2$ was prepared via hydrothermal method with urea-assisted treatment followed by a heating process. First, $\text{MnCl}_2 \cdot 4\text{H}_2\text{O}$, $\text{NiCl}_2 \cdot 6\text{H}_2\text{O}$, $\text{CoCl}_2 \cdot 6\text{H}_2\text{O}$ and $x \text{ g}$ urea ($x = 0 \text{ g}, 0.1 \text{ g}, 0.5 \text{ g}, 1.0 \text{ g}$, molar ratio of $\text{Mn}:\text{Ni}:\text{Co}:\text{urea} = 1:1:1:0, 1.2, 6, 12$) were dissolved in 50 mL mixed solvent ($V_{\text{H}_2\text{O}}:V_{\text{EtOH}} = 1:1$), then treated with ultrasound for about 30 min to form pink solution A. Simultaneously, 5 mmol of NH_4HCO_3 was dissolved in 50 mL mixed solution ($V_{\text{H}_2\text{O}}:V_{\text{EtOH}} = 1:1$) to form solution B. Then, solution B was slowly dropped into solution A to form solution C which was moved into a 150 mL Teflon autoclave followed by a heat treatment at $180 \text{ }^\circ\text{C}$ for 12 h. The product was filtered and washed three times with distilled water and ethanol. After drying at $80 \text{ }^\circ\text{C}$ for 12 h, the black brown precursor was obtained. Then the black brown precursor was fully mixed with a stoichiometric amount of $\text{LiOH}\cdot\text{H}_2\text{O}$ (5% excess). Finally, the mixture was pre-calcined for 5 h at $450 \text{ }^\circ\text{C}$ in muffle furnace and calcined for 12 h after heating to $850 \text{ }^\circ\text{C}$, to obtain the experimental product LNCM-1 (LNCM-0, LNCM-1, LNCM-2, LNCM-3 corresponding to the $\text{LiNi}_{1/3}\text{Co}_{1/3}\text{Mn}_{1/3}\text{O}_2$ sample obtained when urea content was 0, 0.1, 0.5 and 1.0g in the experiment).

2.2. Structural Characterization

The crystallinity and phase purity of as-prepared samples were measured by X-ray diffraction (XRD, Rigaku Smart Lab 3 KW with Cu K α radiation, $\lambda = 1.5406 \text{ \AA}$). Spectra were collected in the 2θ range from 10° to 80° with the scan rate of $10^\circ \text{ min}^{-1}$. The morphology and microstructure were characterized by scanning electron microscopy (SEM) (Hitachi JSM-7800F) with energy-dispersive X-ray spectroscopy (EDX) analysis and transmission electron microscopy (TEM) (JEM-1400, 200 KV). The oxidation states of Ni, Co, Mn in as-prepared samples were identified by X-ray photoelectron spectroscopy (XPS) (Thermo Scientific ESCALAB 250Xi) using 200 W Al K α radiation. All XPS spectra

of samples were corrected using the C1s line at 284.8 eV, pass energy: 160 eV, scan width: 40 eV, vacuum level: 10^{-9} Pa, the number of scans: 1–3.

2.3. Electrochemical Measurements

The electrochemical tests of samples were performed by assembling CR2016 coin cell. The CR2016 coin cell was fabricated by using lithium metal foil as a anode, the as-prepared electrode as a cathode, a Celgard 2400 separator and 1M LiPF₆ mixture with ethylene carbonate (EC)/ethyl methyl carbonate (EMC)/dimethyl carbonate (DMC) (EC:EMC:DMC = 1:1:1 in volume) as electrolyte solution. The as-prepared electrode was prepared by slurry coating, the slurry consists of 80 wt% active materials, 10 wt% carbon black and a certain volume of N-methyl-2-pyrrolidone solvent (include 10 wt% polyvinylidene fluoride). Then the slurry was coated on an aluminum foil current collector, finally dried at 120 °C for 12 h in a vacuum. The charge–discharge properties were tested on a LAND testing system (LAND CT-2001A, Wuhan, China) between 2.5 V and 4.5 V (vs. Li⁺/Li) at different current densities after the assembled coin cells standing for 24 h. Cyclic voltammetry (CV) tests were measured between 2.5 V and 4.5 V (vs. Li⁺/Li) with positive initial scan polarity at 0.1 mV s⁻¹. Electrochemical impedance spectroscopy (EIS) were carried out on CHI760D (Shanghai, China) electrochemical workstation in the frequency range of 0.1 Hz to 100 kHz with 5 mV amplitude for the new assembled cell after standing for 24 h. All of the electrochemical performances were tested at room temperature.

3. Results and Discussion

The crystallinity and phase purity of as-prepared LiNi_{1/3}Co_{1/3}Mn_{1/3}O₂ were identified by XRD patterns (Figure 1). For all four kinds of LNCM structures, the patterns match well with previously reported pure single phase of LiNi_{1/3}Co_{1/3}Mn_{1/3}O₂ that can be indexed as a layered hexagonal α -NaFeO₂ structure (space group: R-3m) without any impurity phase [28,35]. Furthermore, it indicates the amount of urea has no apparent influence on the structure of LiNi_{1/3}Co_{1/3}Mn_{1/3}O₂. The diffraction peaks are narrow and sharp indicate the as-prepared LiNi_{1/3}Co_{1/3}Mn_{1/3}O₂ possesses high crystallinity. Besides, the distinct separation between (006/102) and (108/110) diffraction peaks suggests highly ordered hexagonal layered structure of materials. The degree of cation mixing in crystal lattice are measured by intensity ratio (003) and (104) peaks (I_{003}/I_{104}). And the calculated value of LNCM-0, LNCM-1, LNCM-2, LNCM-3 are 1.24, 1.38, 1.40, 1.30 respectively. When the value of I_{003}/I_{104} is larger than 1.2, it indicates a low cation mixing with lithium ions at the 3a site, transition-metal ions (Ni, Co and Mn) at the 3b site and oxygen ions at the 6c site, but also the presence of Ni²⁺ ions migrating into the Li layers [28,36].

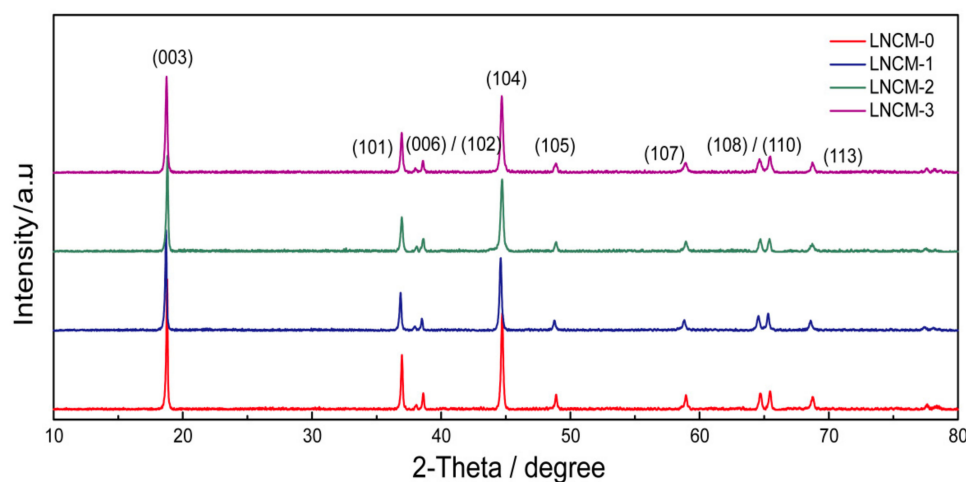


Figure 1. XRD patterns of as-prepared LiNi_{1/3}Co_{1/3}Mn_{1/3}O₂.

The morphology and microstructure of all $\text{LiNi}_{1/3}\text{Co}_{1/3}\text{Mn}_{1/3}\text{O}_2$ were presented in Figure 2a–d. LNCM-0 is made of very small nanoparticles stacked together in the shape of a bowl. LNCM-1 is also formed by the accumulation of very small nanoparticles and part of the upper end of the agglomerated structure is not closed, forming a semi-closed structure, which to some extent shorten diffusion distance of lithium ions and is beneficial to the penetration of electrolyte in its interior while minimize side reactions. With the continuous increase of urea content, some particles of LNCM-2 agglomerate into irregular spheres, with a diameter of about 3–4 μm . When the content of urea further increased, the degree of particle agglomeration further increased and the diameter of LNCM-3 increased to 4–5 μm . Clearly, aggregation and sizes of NCM 111 increase with the addition of urea. The structures of NCM 111 aggregation change from completely open bowl-like (LNCM-0) to enclosed sphere-shaped (LNCM-3). This is because urea decomposes at 160 $^\circ\text{C}$ to produce ammonia gas and carbon dioxide, which may increase the pressure in the Teflon autoclave and the ionic strength of the solution will increase after the gas dissolved in water, making the precursor of NCM 111 more cohesive.

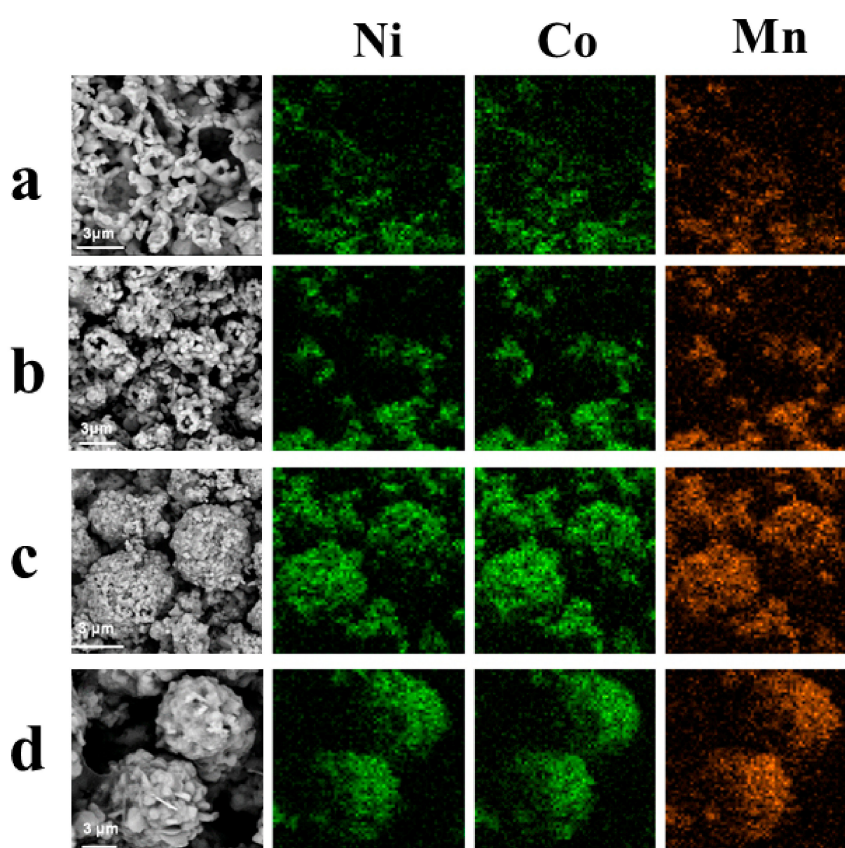


Figure 2. Energy-dispersive X-ray spectroscopy (EDX) patterns for distribution of Ni, Co, Mn on the surface of materials: (a) LNCM-0, (b) LNCM-1, (c) LNCM-2, (d) LNCM-3.

The EDX scanning images of Ni, Co and Mn on the surfaces of LNCM-0, LNCM-1, LNCM-2 and LNCM-3 are shown in Figure 2. From the results of element scanning, it can be seen that Ni, Co and Mn are evenly distributed on the surfaces of LNCM-0, LNCM-1, LNCM-2 and LNCM-3 samples and there is no local accumulation, indicating that the transition metal elements on the surfaces of LNCM-0, LNCM-1, LNCM-2 and LNCM-3 are uniformly distributed. At the same time, it also shows that the amount of urea will not affect the distribution of transition metal elements on the surface of NCM 111, but only affect the degree of mutual agglomeration between particles.

In order to further study the morphological characteristics of LNCM-0, LNCM-1, LNCM-2 and LNCM-3, nitrogen adsorption–desorption isotherms were utilized to analyze the pore size distribution and specific surface area of all samples. As shown in Figure 3, the pore size distribution of LNCM-0,

LNCM-1, LNCM-2 and LNCM-3 center on 4.520, 1.543, 1.543 and 1.475 nm, respectively and the specific surface area of LNCM-0, LNCM-1, LNCM-2, LNCM-3 is $2.0 \text{ m}^2 \text{ g}^{-1}$, $1.2 \text{ m}^2 \text{ g}^{-1}$, $0.9 \text{ m}^2 \text{ g}^{-1}$, $0.6 \text{ m}^2 \text{ g}^{-1}$ respectively. The specific surface area of LNCM-0 with the smallest amount of urea is the largest, followed by LNCM-1 and LNCM-3 with the largest amount of urea is the smallest. The Brunauer–Emmett–Teller (BET) surface area analysis also shows that with the increase of the amount of urea additive in the solvent thermal reaction process, the particles can be agglomerated more closely, resulting in the continuous decrease of the specific surface area of the prepared materials.

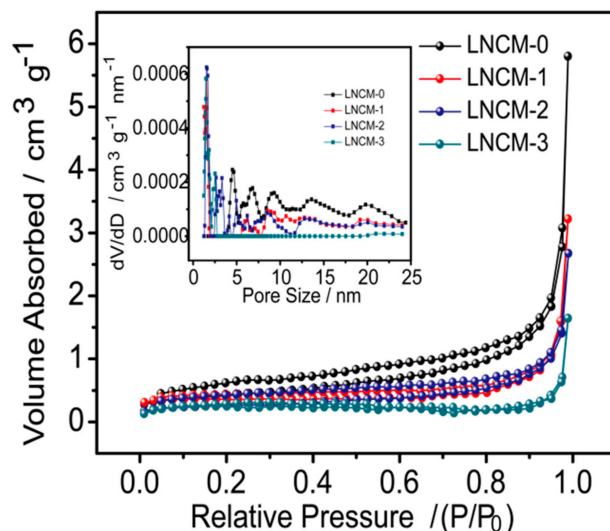


Figure 3. BET: nitrogen adsorption–desorption isotherms of LNCM-0~LNCM-3.

To study the oxidation states of Ni, Co and Mn in samples, LNCM-1 was characterized by X-ray photoelectron spectroscopy (XPS) measurement. As shown in Figure 4a, LNCM-1 is mainly composed of lithium, nickel, cobalt, manganese and oxygen, without other impurity elements. From the Ni2p spectra in Figure 4b, the binding energy values of Ni2p_{3/2} and Ni2p_{1/2} were at approximately 854.7 and 872.4 eV, with a difference of 17.6 eV and three satellite peaks, indicating that the valence of Ni is +2 in LNCM-1. Simultaneously, as can be found from the XPS spectra of Mn2p in Figure 4c, the binding energy displayed by the two main peaks of Mn2p_{3/2} and Mn2p_{1/2} are about 642.2 and 654.0 eV, with a difference of 11.8 eV, indicating that the valence of Mn is +4 in LNCM-1. Similarly, according to the XPS spectra of Co2p in Figure 4d, the binding energy values of Co2p_{3/2} and Co2p_{1/2} are about 780 and 795.1 eV, with the difference of 14.9 eV, indicating that the oxidation state of Co is +3 in LNCM-1. The XPS results are similar to those of reported layered LiNi_{1/3}Co_{1/3}Mn_{1/3}O₂ [37–39]. Therefore, Ni, Co and Mn exist in LNCM-1 as Ni²⁺, Co³⁺ and Mn⁴⁺ respectively, which is consistent with the oxidation states of each element in the ideal target product LiNi_{1/3}Co_{1/3}Mn_{1/3}O₂.

In Figure 5, CV curves of as-prepared LiNi_{1/3}Co_{1/3}Mn_{1/3}O₂ cathodes in the voltage range of 2.5~4.5 V only have one pair of major redox couple and they were appeared in the potential range of 3.55–3.85 V, which correspond to Ni²⁺/Ni⁴⁺ and Co³⁺/Co⁴⁺ [28,40,41]. Additionally, no reduction peak arises below the potential 3.5 V, which indicated no Mn³⁺ exists in as-prepared LiNi_{1/3}Co_{1/3}Mn_{1/3}O₂ samples. From the comparison of CV test results of different samples, it can be seen that LNCM-1 has the highest peak current and the smallest peak voltage interval, indicating that LNCM-1 has the highest electrochemical activity and the best reversible capacity of lithium ions insertion/extraction. And according to CV curves (Figure 6a,c,e,g) of LNCM-0, LNCM-1, LNCM-2, LNCM-3 at various scan rates, with the increase of scanning rate, peak current (I_p) increases continuously and peak voltage difference (ΔV) increases gradually. Because as the scan speed increases, the invertibility of lithium ions insertion/extraction decreases that brings about the decrease of current efficiency. When the sweep speed increased to 1 mV s^{-1} , no other redox peak appeared in the voltage range of 2.5 ~ 4.5 V, indicating that NCM 111 in the electrode was stable.

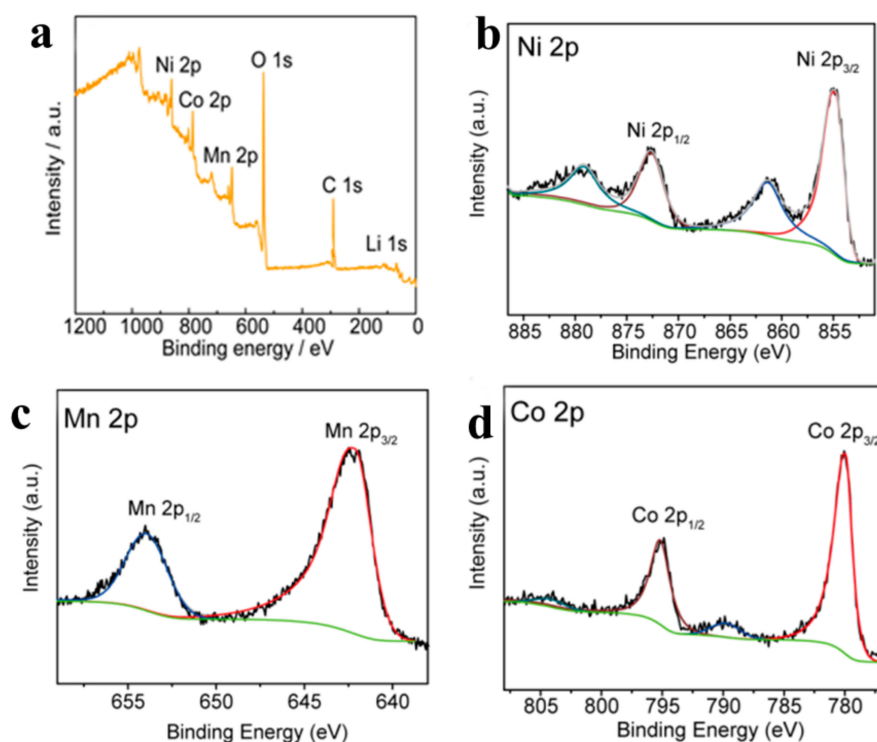


Figure 4. XPS spectra of LNCM-1: (a) full XPS spectra, (b) Ni 2p, (c) Mn 2p, (d) Co 2p.

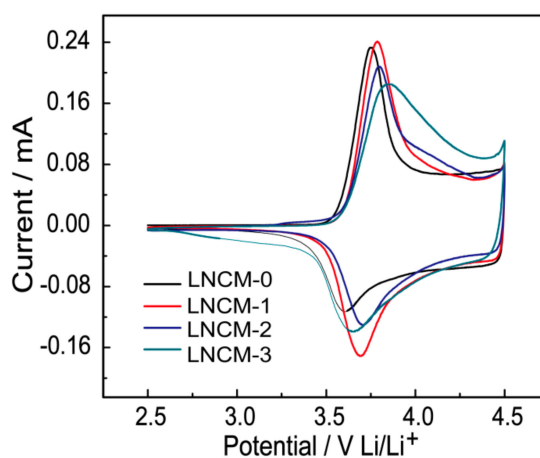


Figure 5. Cyclic voltammetry (CV) curves of LNCM-0~LNCM-3 cathodes at a scan rate of 0.1 mV s^{-1} .

Figure 6b,d,f,h shows the relationship between I_p and $V^{1/2}$ of LNCM-0, LNCM-1, LNCM-2 and LNCM-3 cathode materials. The diffusion coefficient of lithium ions (D_{Li}) can be calculated by Randles–Sevcik equation [42].

$$I_p = 2.69 \times 10^5 n^{3/2} A D_{Li}^{1/2} C V^{1/2} \quad (1)$$

In the equation, I_p (A) is the peak current, n is the electrons transfer during per redox reaction, A (cm^2) is the electrode effective area, D_{Li} ($\text{cm}^2 \cdot \text{s}^{-1}$) is the diffusion coefficient of lithium ions, C ($\text{mol} \cdot \text{cm}^{-3}$) is the Li^+ concentration inside the electrode, V ($\text{V} \cdot \text{s}^{-1}$) is the scan rate. After calculation, the D_{Li} value of LNCM-0, LNCM-1, LNCM-2, LNCM-3 is 1.81×10^{-8} , 2.77×10^{-8} , 2.03×10^{-8} , $1.79 \times 10^{-8} \text{ cm}^2 \cdot \text{s}^{-1}$ respectively. The D_{Li} value of LNCM-1 is the largest, while LNCM-3 is smallest, indicating that the diffusion rate of lithium ions was the fastest in the semi-closed LNCM-1 and the slowest in the spherical LNCM-3 positive electrode. As a faster diffusion rate of lithium ions makes a smaller

polarization effect of the electrode due to the increase of current density lead to a better rate capability, it is not difficult infer semi-closed $\text{LiNi}_{1/3}\text{Co}_{1/3}\text{Mn}_{1/3}\text{O}_2$ has excellent rate capability.

Electrochemical impedance spectroscopy (EIS) was also tested to measure the electrochemical capability of $\text{LiNi}_{1/3}\text{Co}_{1/3}\text{Mn}_{1/3}\text{O}_2$ cathodes (Figure 7). EIS graph is composed of high and intermediate frequency semicircle and low frequency oblique line. The slope of the oblique line to a certain extent reflects the lithium ion diffusion ability inside material. The higher the slope, the stronger the diffusion capacity of lithium ions. It is easy to be found from EIS curves that lithium ions diffuse fastest in the semi-closed LNCM-1 among all samples. In fitting equivalent circuit, R_e corresponds to the internal resistance of the cell, including the internal resistance of the material and other components of the battery; R_s corresponds to the resistance of surface electrochemical interface (SEI); R_{ct} is the resistance of charge transfer, which refers to the resistance of electrons and lithium ions in the process of charge transfer at the conductive junction; Z_w corresponds to the Warburg impedance, representing the diffusion of lithium ions in solid particles. After equivalent fitting calculation, the R_{ct} for semi-closed LNCM-1 cathode is 73.6Ω while other three $\text{LiNi}_{1/3}\text{Co}_{1/3}\text{Mn}_{1/3}\text{O}_2$ cathodes are about 130Ω . Summing up EIS data in Figure 7, the semi-closed LNCM-1 has the best conductivity and highest electrochemical activity. Results of EIS test are consistent with the CV curve and charge–discharge test data.

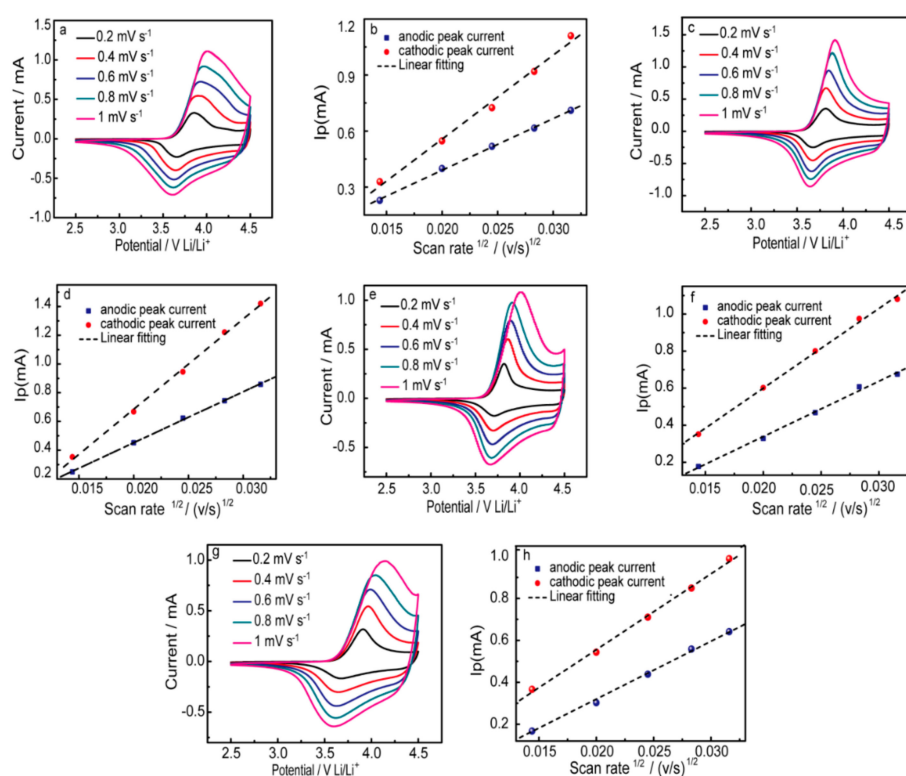


Figure 6. (a,c,e,g) CV curves of LNCM-0, LNCM-1, LNCM-2, LNCM-3 cathodes at a sweep rate of $0.2\text{--}1 \text{ mV s}^{-1}$, (b,d,f,h) relationship between peak current I_p and square root of sweep speed ($V^{1/2}$) of LNCM-0, LNCM-1, LNCM-2, LNCM-3 cathodes.

The electrochemical measurement is a critical evidence for evaluating cathode materials. As shown in Figure 8a the initial discharge capacity of LNCM-0, LNCM-1, LNCM-2, LNCM-3 cathodes at $0.17 \text{ A}\cdot\text{g}^{-1}$ in the voltage range from 2.5 to 4.5 V is $159 \text{ mAh}\cdot\text{g}^{-1}$, $167 \text{ mAh}\cdot\text{g}^{-1}$, $153.7 \text{ mAh}\cdot\text{g}^{-1}$, $145 \text{ mAh}\cdot\text{g}^{-1}$, respectively. The charging platforms gradually increase with the addition of urea consumption and the operating voltage platform is 3.65 – 3.8 V. Among these samples, LNCM-1 displayed the highest discharge capacity of $167 \text{ mAh}\cdot\text{g}^{-1}$ with an initial coulombic efficiency of 87.9%. However, LNCM-3 had the lowest discharge capacity of $145 \text{ mAh}\cdot\text{g}^{-1}$ with an initial coulombic efficiency of 80.6% at $0.17 \text{ A}\cdot\text{g}^{-1}$. This result could be attributed to particles agglomerate more tightly

with the increasing of urea added, resulting in the decrease of its specific surface area, which makes it difficult for the electrolyte to penetrate into the interior of structures and the diffusion distance of Li^+ increases, so the discharge capacity of LNCM-3 decreases. As cycle performance at $0.34 \text{ A}\cdot\text{g}^{-1}$ shown in Figure 8b, LNCM-1 with an initial discharge capacity of $157.7 \text{ mAh}\cdot\text{g}^{-1}$ but $130 \text{ mAh}\cdot\text{g}^{-1}$ after 100 cycles. However, the discharge capacity of LNCM-0 decreases quickly but remains 34.82% of initial after 80 cycles. This may be because of the bowl-shaped morphology of LNCM-0 has more side reactions and damage of structure are much more serious. This result shows that the addition of urea can significantly improve the cycling performance of NCM 111.

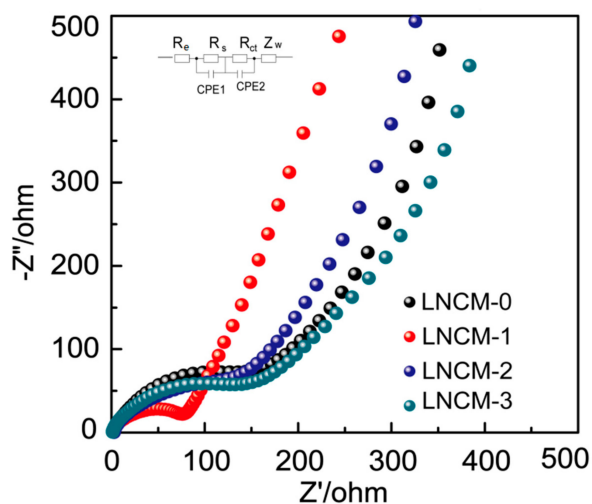


Figure 7. Electrochemical impedance spectroscopy (EIS) curves of LNCM-0~LNCM-3 cathodes in the frequency range of 0.1 Hz to 100 kHz.

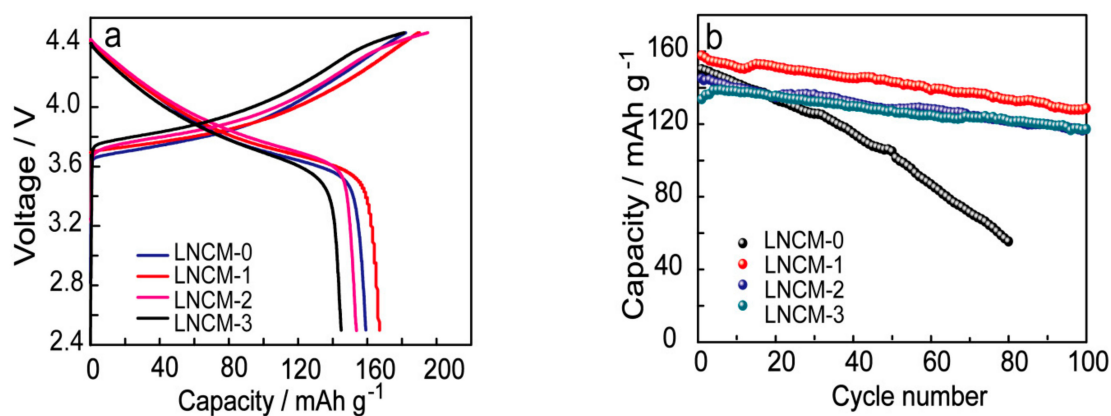


Figure 8. Charge and discharge characteristics of LNCM-0~LNCM-3: (a) discharge capacity at $0.17 \text{ A}\cdot\text{g}^{-1}$, (b) cycle performance at $0.34 \text{ A}\cdot\text{g}^{-1}$.

According to Figure 8, LNCM-1 has the highest discharge capacity and the best cycling performance, so the electrochemical performances of LNCM-1 were further tested. As shown in Figure 9a, the initial discharge capacities of LNCM-1 are 169.6 , 167 , 157.7 , 140.9 and $114.3 \text{ mAh}\cdot\text{g}^{-1}$ corresponding to 0.034 , 0.17 , 0.34 , 0.85 and $1.7 \text{ A}\cdot\text{g}^{-1}$ respectively. It is worth noting that LNCM-1 can still achieve very high discharge capacities at high current density. The capacity at current densities of $0.85 \text{ A}\cdot\text{g}^{-1}$ and $1.7 \text{ A}\cdot\text{g}^{-1}$ is 84.37% and 68.44% of $0.17 \text{ A}\cdot\text{g}^{-1}$, respectively. As shown in Figure 9b, after 100 cycles, the discharge capacities maintain about $120 \text{ mAh}\cdot\text{g}^{-1}$ at $0.85 \text{ A}\cdot\text{g}^{-1}$ and $100 \text{ mAh}\cdot\text{g}^{-1}$ at $1.7 \text{ A}\cdot\text{g}^{-1}$, respectively, reflecting that LNCM-1 still has excellent cycling performance at high charge–discharge current densities, which is of certain significance for quick charging of batteries. From Figure 9c, it can be found that the discharge capacity of LNCM-1 at different current densities of 0.17 , 0.34 ,

0.85, 1.19 and $1.7 \text{ A}\cdot\text{g}^{-1}$ has little difference. When the discharge current density recovers from high value of 1.7 to $0.17 \text{ A}\cdot\text{g}^{-1}$, it is still close to the initial discharge capacity, reflecting the excellent rate capability of LNCM-1. There are discharge capacity differences between Figure 9a–c at $1.7 \text{ A}\cdot\text{g}^{-1}$, as shown in Figure 9b the discharge capacity gradually rises in the first few cycles until approaches $120 \text{ mAh}\cdot\text{g}^{-1}$ and the reason might be the polarization differences caused by incomplete activation and mass of samples.

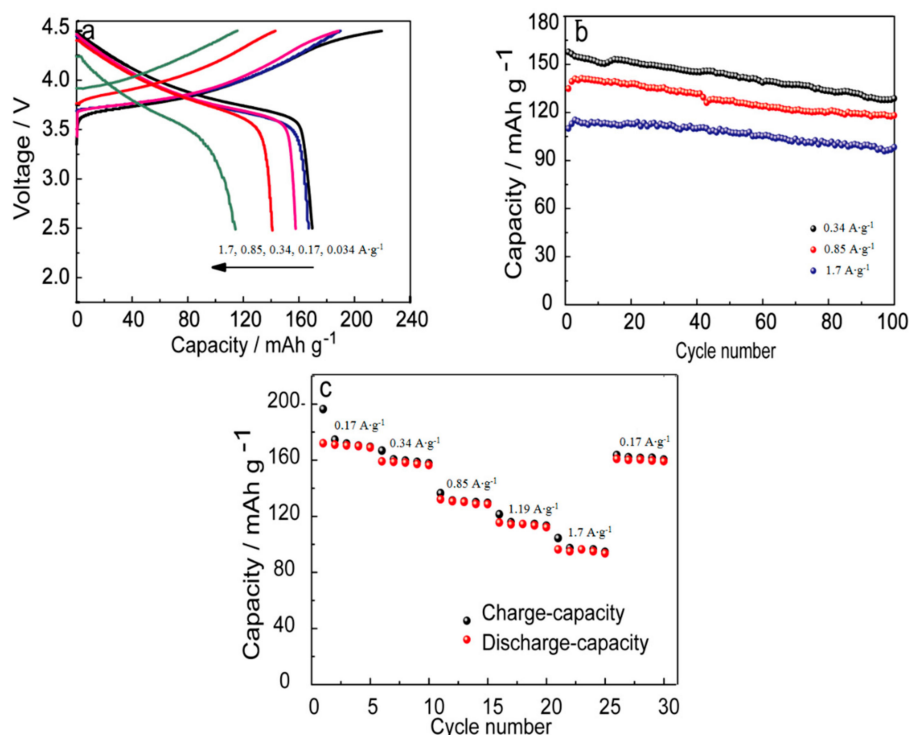


Figure 9. Charge and discharge characteristics of LNCM-1: (a) Charge-discharge curve at $0.034, 0.17, 0.34, 0.85$ and $1.7 \text{ A}\cdot\text{g}^{-1}$ in the voltage range of $2.5\sim 4.5 \text{ V}$, (b) cycle performance at $0.34, 0.85$ and $1.7 \text{ A}\cdot\text{g}^{-1}$ in the voltage range of $2.5\sim 4.5 \text{ V}$, (c) rate performance.

In our opinion, the possible reasons the influence of the morphology of $\text{LiNi}_{1/3}\text{Co}_{1/3}\text{Mn}_{1/3}\text{O}_2$ on its electrochemical performance are as follows. First, as the average particle size of conductive carbon black is tens of nanometers while the pore diameter of bowl-like and semi-closed samples is on the micrometer scale and there is no obvious hole at closed sample, it can be speculated that the conductive carbon black is more easily mixed into the interior of the open and semi-closed materials. Secondly, the open and semi-closed structure makes material a wider contact area with the electrolyte, which have more active sites. Especially in semi-closed structure the lithium ion migration is faster due to a wide ion transport network shorten the diffusion path of lithium ions in materials. Conversely, electrolyte penetrates into the internal of the spherical material slowly, many reactions only occur in the surface caused by the electron have no time to react with the inner active materials when the current density increases, resulting in charge accumulation and the polarization increases on the surface of electrode. Finally, specific surface area of samples does not mean larger is better. When the specific surface area increases, more SEI are generated. The formation of SEI not only consumes the active substances, but also increases the electrode resistance. In addition, the increase of specific surface area will bring more side reactions, easily damaging the structure of $\text{LiNi}_{1/3}\text{Co}_{1/3}\text{Mn}_{1/3}\text{O}_2$ and affecting the cycling performance.

4. Conclusions

In conclusion, by controlling the addition amount of urea, the particle agglomeration degree, contact area with electrolyte and charge–discharge of NCM 111 can be effectively controlled. It is found that for the semi-closed lithium ion diffusion rate is the fastest, conductivity and high rate performance is the best. a three-dimensional semi-closed NCM 111 has been successful designed, which exhibited a high rate capability with a specific capacity of $114.3 \text{ mAh}\cdot\text{g}^{-1}$ and considerable cycle life with 89.3% capacity retention after 100 cycles at $1.7 \text{ A}\cdot\text{g}^{-1}$. It mainly benefits from a semi-closed structure that could facilitating the penetration of electrolyte, constructing a wide ion transport network, resulting in more active sites and shorting the diffusion path, thus reducing the polarization during the charge–discharge process at high current density while the side reactions are effectively controlled. Thus, this way could be served as an effective strategy for designing high performance layered-cathode material that affords high power density for Li-ion battery in practical application. In order to further determine the cause of the change of sample morphology, our further work is to study the effects of pressure and ion strength in hydrothermal treatment on the morphology of the synthesized samples.

Author Contributions: J.-P.H. and Q.D. conceived and designed the experiments; J.-P.H. and J.-J.L. performed the experiments; J.-P.H., Q.M., J.L. and H.S. analyzed the data; X.-W.W. and Y.-P.W. contributed reagents/materials/analysis tools; J.-P.H. wrote the paper. All authors have read and agreed to the published version of the manuscript.

Acknowledgments: This work was supported by the Ministry of Science and Technology of the People’s Republic of China (Grant No. 2016YFA0202500), the National Natural Science Foundation of China (Grant No.51772093), the National key Research and Development Program of China (2017YFD0301507), the Double First-Class Construction Project of Hunan Agricultural University (Grant no. SYL201802002, SYL201802008), the Science and Technology Department of Hunan Province (Grant no.2018RS3086), the Distinguished Youth Foundation of Hunan Province (Grant no 2019JJ20010) and the “1515” Talent Cultivation Plan of Hunan Agricultural University.

Conflicts of Interest: The authors declare that they have no conflict of interest.

References

1. Guo, Y.-G.; Chen, J. Special topic on electrochemical power sources. *Sci. China Chem.* **2017**, *60*, 1481–1482. [[CrossRef](#)]
2. Winter, M.; Barnett, B.; Xu, K. Before Li Ion Batteries. *Chem. Rev.* **2018**, *118*, 11433–11456. [[CrossRef](#)]
3. Bock, R.; Onsrud, M.; Karoliussen, H.; Pollet, B.G.; Seland, F.; Burheim, O.S. Thermal Gradients with Sintered Solid State Electrolytes in Lithium-Ion Batteries. *Energies* **2020**, *13*, 253. [[CrossRef](#)]
4. Li, M.; Lu, J.; Chen, Z.; Amine, K. 30 Years of Lithium-Ion Batteries. *Adv. Mater.* **2018**, *30*, 1800561. [[CrossRef](#)] [[PubMed](#)]
5. Armand, M.; Tarascon, J.M. Building better batteries. *Nature* **2008**, *451*, 652–657. [[CrossRef](#)] [[PubMed](#)]
6. Lu, Z.; MacNeil, D.D.; Dahn, J.R. Layered $\text{Li}[\text{Ni}_x\text{Co}_{1-2x}\text{Mn}_x]\text{O}_2$ Cathode Materials for Lithium-Ion Batteries. *Electrochem. Solid-State Lett.* **2001**, *4*, A200–A203. [[CrossRef](#)]
7. MacNeil, D.D.; Lu, Z.; Dahn, J.R. Structure and Electrochemistry of $\text{Li}[\text{Ni}_x\text{Co}_{1-2x}\text{Mn}_x]\text{O}_2$ ($0 \leq x \leq 1/2$). *J. Electrochem. Soc.* **2002**, *149*, A1332–A1336. [[CrossRef](#)]
8. Zhang, N.; Zaker, N.; Li, H.; Liu, A.; Inglis, J.; Jing, L.; Li, J.; Li, Y.; Botton, G.A.; Dahn, J.R. Cobalt-Free Nickel-Rich Positive Electrode Materials with a Core–Shell Structure. *Chem. Mater.* **2019**, *31*, 10150–10160. [[CrossRef](#)]
9. Li, H.; Liu, A.; Zhang, N.; Wang, Y.; Yin, S.; Wu, H.; Dahn, J.R. An Unavoidable Challenge for Ni-Rich Positive Electrode Materials for Lithium-Ion Batteries. *Chem. Mater.* **2019**, *31*, 7574–7583. [[CrossRef](#)]
10. Beletskii, E.V.; Alekseeva, E.V.; Spiridonova, D.Y.V.; Yankin, A.N.; Levin, O.V. Overcharge Cycling Effect on the Surface Layers and Crystalline Structure of LiFePO_4 Cathodes of Li-Ion Batteries. *Energies* **2019**, *12*, 4652. [[CrossRef](#)]
11. Zhang, J.; Guo, X.; Yao, S.; Qiu, X. High capacity lithium-manganese-nickel-oxide composite cathodes with low irreversible capacity loss and good cycle life for lithium ion batteries. *Sci. China Chem.* **2016**, *59*, 1479–1485. [[CrossRef](#)]

12. Lee, W.; Muhammad, S.; Kim, T.; Kim, H.; Lee, E.; Jeong, M.; Son, S.; Ryou, J.-H.; Yoon, W.-S. New Insight into Ni-Rich Layered Structure for Next-Generation Li Rechargeable Batteries. *Adv. Energy Mater.* **2018**, *8*, 1701788. [[CrossRef](#)]
13. Ahn, Y.-K.; Jo, Y.N.; Cho, W.; Yu, J.-S.; Kim, K.J. Mechanism of Capacity Fading in the LiNi_{0.8}Co_{0.1}Mn_{0.1}O₂ Cathode Material for Lithium-Ion Batteries. *Energies* **2019**, *12*, 1638. [[CrossRef](#)]
14. Wang, L.; Maxisch, T.; Ceder, G. A First-Principles Approach to Studying the Thermal Stability of Oxide Cathode Materials. *Chem. Mater.* **2007**, *19*, 543–552. [[CrossRef](#)]
15. Yudha, C.S.; Muzayanha, S.U.; Widiyandari, H.; Iskandar, F.; Sutopo, W.; Purwanto, A. Synthesis of LiNi_{0.85}Co_{0.14}Al_{0.01}O₂ Cathode Material and its Performance in an NCA/Graphite Full-Battery. *Energies* **2019**, *12*, 1886. [[CrossRef](#)]
16. Noh, H.-J.; Youn, S.; Yoon, C.S.; Sun, Y.-K. Comparison of the structural and electrochemical properties of layered Li[Ni_xCoyMnz]O₂ (x = 1/3, 0.5, 0.6, 0.7, 0.8 and 0.85) cathode material for lithium-ion batteries. *J. Power Sources* **2013**, *233*, 121–130. [[CrossRef](#)]
17. Yao, W.; Liu, Y.; Li, D.; Zhang, Q.; Zhong, S.; Cheng, H.; Yan, Z. Synergistically Enhanced Electrochemical Performance of Ni-rich Cathode Materials for Lithium-ion Batteries by K and Ti Co-modification. *J. Phys. Chem. C* **2020**, *124*, 2346–2356. [[CrossRef](#)]
18. Fan, X.; Hu, G.; Zhang, B.; Ou, X.; Zhang, J.; Zhao, W.; Jia, H.; Zou, L.; Li, P.; Yang, Y. Crack-free single-crystalline Ni-rich layered NCM cathode enable superior cycling performance of lithium-ion batteries. *Nano Energy* **2020**, *70*, 104450. [[CrossRef](#)]
19. Zhang, X.-D.; Shi, J.-L.; Liang, J.-Y.; Yin, Y.-X.; Guo, Y.-G.; Wan, L.-J. Structurally modulated Li-rich cathode materials through cooperative cation doping and anion hybridization. *Sci. China Chem.* **2017**, *60*, 1554–1560. [[CrossRef](#)]
20. Jung, S.-K.; Gwon, H.; Hong, J.; Park, K.-Y.; Seo, D.-H.; Kim, H.; Hyun, J.; Yang, W.; Kang, K. Understanding the Degradation Mechanisms of LiNi_{0.5}Co_{0.2}Mn_{0.3}O₂ Cathode Material in Lithium Ion Batteries. *Adv. Energy Mater.* **2014**, *4*, 1300787. [[CrossRef](#)]
21. Heubner, C.; Nickol, A.; Seeba, J.; Reuber, S.; Junker, N.; Wolter, M.; Schneider, M.; Michaelis, A. Understanding thickness and porosity effects on the electrochemical performance of LiNi_{0.6}Co_{0.2}Mn_{0.2}O₂-based cathodes for high energy Li-ion batteries. *J. Power Sources* **2019**, *419*, 119–126. [[CrossRef](#)]
22. Li, G.; Liu, Z.; Wang, D.; He, X.; Liu, S.; Gao, Y.; AlZahrani, A.; Kim, S.H.; Chen, L.-Q.; Wang, D. Electrokinetic Phenomena Enhanced Lithium-Ion Transport in Leaky Film for Stable Lithium Metal Anodes. *Adv. Energy Mater.* **2019**, *9*, 1900704. [[CrossRef](#)]
23. Qi, R.; Shi, J.-L.; Zhang, X.-D.; Zeng, X.-X.; Yin, Y.-X.; Xu, J.; Chen, L.; Fu, W.-G.; Guo, Y.-G.; Wan, L.-J. Improving the stability of LiNi_{0.80}Co_{0.15}Al_{0.05}O₂ by AlPO₄ nanocoating for lithium-ion batteries. *Sci. China Chem.* **2017**, *60*, 1230–1235. [[CrossRef](#)]
24. Shi, J.-L.; Xiao, D.-D.; Ge, M.; Yu, X.; Chu, Y.; Huang, X.; Zhang, X.-D.; Yin, Y.-X.; Yang, X.-Q.; Guo, Y.-G.; et al. High-Capacity Cathode Material with High Voltage for Li-Ion Batteries. *Adv. Mater.* **2018**, *30*, 1705575. [[CrossRef](#)]
25. Fang, Y.; Huang, Y.; Tong, W.; Cai, Y.; Wang, X.; Guo, Y.; Jia, D.; Zong, J. Synthesis of hollow peanut-like hierarchical mesoporous LiNi_{1/3}Co_{1/3}Mn_{1/3}O₂ cathode materials with exceptional cycle performance for lithium-ion batteries by a simple self-template solid-state method. *J. Alloys Compd.* **2018**, *743*, 707–715. [[CrossRef](#)]
26. Fu, F.; Xu, G.-L.; Wang, Q.; Deng, Y.-P.; Li, X.; Li, J.-T.; Huang, L.; Sun, S.-G. Synthesis of single crystalline hexagonal nanobricks of LiNi_{1/3}Co_{1/3}Mn_{1/3}O₂ with high percentage of exposed {010} active facets as high rate performance cathode material for lithium-ion battery. *J. Mater. Chem. A* **2013**, *1*, 3860–3864. [[CrossRef](#)]
27. Wang, F.; Xiao, S.; Chang, Z.; Yang, Y.; Wu, Y. Nanoporous LiNi_{1/3}Co_{1/3}Mn_{1/3}O₂ as an ultra-fast charge cathode material for aqueous rechargeable lithium batteries. *Chem. Commun.* **2013**, *49*, 9209–9211. [[CrossRef](#)]
28. Peng, L.; Zhu, Y.; Khakoo, U.; Chen, D.; Yu, G. Self-assembled LiNi_{1/3}Co_{1/3}Mn_{1/3}O₂ nanosheet cathodes with tunable rate capability. *Nano Energy* **2015**, *17*, 36–42. [[CrossRef](#)]
29. Zheng, H.; Chen, X.; Yang, Y.; Li, L.; Li, G.; Guo, Z.; Feng, C. Self-Assembled LiNi_{1/3}Co_{1/3}Mn_{1/3}O₂ Nanosheet Cathode with High Electrochemical Performance. *ACS Appl. Mater. Interfaces* **2017**, *9*, 39560–39568. [[CrossRef](#)]
30. Huang, Q.; Ma, L.; Liu, A.; Ma, X.; Li, J.; Wang, J.; Dahn, J.R. The reactivity of charged positive Li_{1-n}[Ni_xMnyCo_z]O₂ electrodes with electrolyte at elevated temperatures using accelerating rate calorimetry. *J. Power Sources* **2018**, *390*, 78–86. [[CrossRef](#)]

31. Accardo, G.; Spiridigliozzi, L.; Cioffi, R.; Ferone, C.; Di Bartolomeo, E.; Yoon, S.P.; Dell'Agli, G. Gadolinium-doped ceria nanopowders synthesized by urea-based homogeneous co-precipitation (UBHP). *Mater. Chem. Phys.* **2017**, *187*, 149–155. [[CrossRef](#)]
32. Dell'Agli, G.; Spiridigliozzi, L.; Pansini, M.; Accardo, G.; Yoon, S.P.; Frattini, D. Effect of the carbonate environment on morphology and sintering behaviour of variously co-doped (Ca, Sr, Er, Pr) Samarium-doped Ceria in co-precipitation/hydrothermal synthesis. *Ceram. Int.* **2018**, *44*, 17935–17944. [[CrossRef](#)]
33. Spiridigliozzi, L.; Ferone, C.; Cioffi, R.; Accardo, G.; Frattini, D.; Dell'Agli, G. Entropy-Stabilized Oxides owning Fluorite Structure obtained by Hydrothermal Treatment. *Materials* **2020**, *13*, 558. [[CrossRef](#)] [[PubMed](#)]
34. Spiridigliozzi, L.; Ferone, C.; Cioffi, R.; Bortolotti, M.; Dell'Agli, G. New Insights in the Hydrothermal Synthesis of Rare-Earth Carbonates. *Materials* **2019**, *12*, 2062. [[CrossRef](#)]
35. Wei, G.-Z.; Lu, X.; Ke, F.-S.; Huang, L.; Li, J.-T.; Wang, Z.-X.; Zhou, Z.-Y.; Sun, S.-G. Crystal Habit-Tuned Nanoplate Material of $\text{Li}[\text{Li}_{1/3-2x/3}\text{Ni}_x\text{Mn}_{2/3-x/3}]\text{O}_2$ for High-Rate Performance Lithium-Ion Batteries. *Adv. Mater.* **2010**, *22*, 4364–4367. [[CrossRef](#)]
36. Hwang, B.J.; Tsai, Y.W.; Carlier, D.; Ceder, G. A Combined Computational/Experimental Study on $\text{LiNi}_{1/3}\text{Co}_{1/3}\text{Mn}_{1/3}\text{O}_2$. *Chem. Mater.* **2003**, *15*, 3676–3682. [[CrossRef](#)]
37. Zhang, Y.; Jia, D.; Tang, Y.; Huang, Y.; Pang, W.; Guo, Z.; Zhou, Z. In Situ Chelating Synthesis of Hierarchical $\text{LiNi}_{1/3}\text{Co}_{1/3}\text{Mn}_{1/3}\text{O}_2$ Polyhedron Assemblies with Ultralong Cycle Life for Li-Ion Batteries. *Small* **2018**, *14*, 1704354. [[CrossRef](#)]
38. Li, Z.; Du, F.; Bie, X.; Zhang, D.; Cai, Y.; Cui, X.; Wang, C.; Chen, G.; Wei, Y. Electrochemical Kinetics of the $\text{Li}[\text{Li}_{0.23}\text{Co}_{0.3}\text{Mn}_{0.47}]\text{O}_2$ Cathode Material Studied by GITT and EIS. *J. Phys. Chem. C* **2010**, *114*, 22751–22757. [[CrossRef](#)]
39. Li, J.; Xiong, S.; Liu, Y.; Ju, Z.; Qian, Y. Uniform $\text{LiNi}_{1/3}\text{Co}_{1/3}\text{Mn}_{1/3}\text{O}_2$ hollow microspheres: Designed synthesis, topotactical structural transformation and their enhanced electrochemical performance. *Nano Energy* **2013**, *2*, 1249–1260. [[CrossRef](#)]
40. Shaju, K.M.; Subba Rao, G.V.; Chowdari, B.V.R. Performance of layered $\text{Li}(\text{Ni}_{1/3}\text{Co}_{1/3}\text{Mn}_{1/3})\text{O}_2$ as cathode for Li-ion batteries. *Electrochim. Acta* **2002**, *48*, 145–151. [[CrossRef](#)]
41. Kim, J.-M.; Chung, H.-T. Role of transition metals in layered $\text{Li}[\text{Ni},\text{Co},\text{Mn}]\text{O}_2$ under electrochemical operation. *Electrochim. Acta* **2004**, *49*, 3573–3580. [[CrossRef](#)]
42. Chen, Z.; Wang, J.; Chao, D.; Baikie, T.; Bai, L.; Chen, S.; Zhao, Y.; Sum, T.C.; Lin, J.; Shen, Z. Hierarchical Porous $\text{LiNi}_{1/3}\text{Co}_{1/3}\text{Mn}_{1/3}\text{O}_2$ Nano-/Micro Spherical Cathode Material: Minimized Cation Mixing and Improved Li^+ Mobility for Enhanced Electrochemical Performance. *Sci. Rep.* **2016**, *6*, 25771. [[CrossRef](#)] [[PubMed](#)]

